FDG PET and Dual-Head Gamma Camera Positron Coincidence Detection Imaging of Suspected Malignancies and Brain Disorders

Dominique Delbeke, James A. Patton, William H. Martin and Martin P. Sandler

Section of Nuclear Medicine, Department of Radiology and Radiological Sciences, Vanderbilt University Medical Center, Nashville, Tennessee

The purpose of the study was to compare the diagnostic accuracy of fluorodeoxyglucose (FDG) images obtained with a dual-head coincidence gamma camera (DHC) with those obtained with a dedicated PET in a series of 26 patients. **Methods:** Nineteen patients with known or suspected malignancies and 7 patients with neurological disorders underwent PET imaging after injection of approximately 10 mCi of FDG. Whole-body imaging was performed on 19 patients and brain imaging on 7 patients. DHC images were then acquired for 30 min over the region of interest using a dual-head gamma camera equipped with ⅜-in.-thick NaI(Tl) crystals and parallel slit-hole collimators. The images were reconstructed in the normal mode, using photopeak/photopeak, photopeak/Compton and Compton/photopeak coincidence events. **Results:** Although the spatial resolutions of PET with a dedicated PET scanner and of DHC are in the same range, the lesion detectability remains superior with PET (4 mm for PET versus 13.5 mm for DHC in phantom experiments) with a contrast ratio of 5:1. This is most probably attributable to the higher sensitivity of PET (2238 coincidences/min/μCi for PET versus 89 coincidences/min/μCi for DHC). The pattern of uptake and interpretation for brain imaging was similar on both PET and DHC images in all patients. In the 19 oncology patients, 38 lesions ranging from 0.7 to 5 cm were detected by PET. DHC imaging detected 28 (73%) of these lesions. Among the 10 lesions not seen with DHC, 5 were less than 1.2 cm, 2 were located centrally within the liver and suffered from marked attenuation effects and 3 were adjacent to regions with high physiological activity. The nondetectability of some lesions with DHC compared with PET can be explained by several factors: (a) start of imaging time (mean ± SD: 73 ± 16 min for PET versus 115 ± 68 min for DHC, leading to FDG decay to 6.75 mCi for PET and 5.2 mCi for DHC); (b) limited efficiency of a ⅜-inch-thick NaI(Tl) crystal to detect ^{18}F photons; (c) suboptimal two-dimensional reconstruction algorithm; and (d) absence of soft-tissue attenuation correction for centrally located lesions. **Conclusion:** FDG DHC imaging is a promising technique for oncological and brain imaging.

Key Words: emission CT; fluorine; neoplasms

J Nucl Med 1999; 40:110–117

High-resolution imaging of 2-[^{18}F]fluoro-2-deoxy-D-glucose (FDG) has been used for many years to study glucose utilization in the brain, heart and neoplasms, and the clinical utility of PET is well documented. Initial work involved study of cerebral metabolism of FDG in the evaluation of seizure disorders, brain tumors and dementia (*1–3*). Studies of cardiac metabolism were later used to identify patients with injured but viable myocardium that would benefit from revascularization procedures (*4–6*). Recently, tumor metabolism studies have been performed to identify malignant lesions and evaluate their response to therapy (*7*).

Even though it has been shown that PET may be cost effective because of its impact on patient management (*8–10*), implementation of clinical PET has been hindered by the high cost of PET systems, the need for immediate access to a source of FDG (i.e., a cyclotron and support laboratory near the site of use) because of its 110-min half-life, high maintenance and operating expenses of the scanner and cyclotron and limited reimbursement for clinical procedures by third-party payers. These combined factors have resulted in the development by manufacturers of gamma camera systems capable of performing positron imaging. Previous studies have shown that FDG imaging using SPECT and a conventional gamma camera fitted with an ultra-energy collimator (*11–19*) is feasible. However, FDG SPECT imaging has limited sensitivity and resolution compared with FDG PET imaging (*17*). Therefore, manufacturers have developed dual-head gamma cameras (DHCs) that operate in the coincidence mode in an effort to improve both the sensitivity and resolution of FDG imaging. The purpose of this study was to compare positron coincidence detection images obtained with a DHC and with a dedicated PET scanner in patients with various malignancies or neurological disorders.

METHODS

Equipment and Physical Measurements

Imaging was performed using a DHC with ⅜-in.-thick NaI(Tl) crystals and rectangular field of view detectors with a field of view

Received Dec. 5, 1997; revision accepted Apr. 30, 1998.

For correspondence or reprints contact: Dominique Delbeke, MD, PhD, Department of Radiology and Radiological Sciences, Vanderbilt University Medical Center, 21st Ave. South and Garland, Nashville, TN 37232–2675.

of 38 × 50 cm (VariCam; Elscint, Inc., Hackensack, NJ). The detectors are positioned at 180°, and electronic collimation (coincidence timing window) is used to simultaneously detect in each detector one annihilation photon resulting from a positron decay. Data acquisition is accomplished using the slip ring technology of the VariCam with 3-min rotations used for this evaluation to minimize the effects of radioisotope decay (i.e., 10 rotations for a 30-min acquisition). A 15-ns timing window is used to detect coincidence events, and an offset 45-ns window is used to monitor random coincidence events. Slit collimators (septa of 40 × 4 mm and 10-mm spacing) with graded absorbers (zinc, lead and copper) are used to reduce the singles rate from activity outside of the field of view and to reduce the effects of scattered radiation. Each detector has four pulse height analyzer (PHA) windows (one photopeak and three scatter), permitting flexibility in evaluating combinations of coincidence events detected by photopeak and Compton scatter interactions in the image reconstruction process.

Image reconstruction was accomplished after acquisition was completed by rebinning the data into 90 planar projection arrays corresponding to 180° (note that the second 180° is redundant in coincidence imaging). The rebinning process typically requires about 5 min. The planar projection data are then used to generate tomographic images using standard filtered backprojection algorithms. Before the rebinning process is initiated, two options are available for evaluation purposes. The first option is the ability to select the maximum angle that the path of a photon makes with the crystal that is accepted in the rebinning process (the higher the acceptance angle, the greater the sensitivity at the cost of slightly degraded spatial resolution). A 35° acceptance angle in the transaxial direction was used in this study. The acceptance angle in the axial direction was fixed at 8°. The second option permits the selection of three combinations of PHA windows to be used in the rebinning process. A high-resolution mode uses only photopeak interactions in each detector; a medium resolution, medium sensitivity (NOR) mode adds photopeak interactions in one detector and single Compton interactions in the other; and a high sensitivity mode adds single Compton interactions in each detector. The NOR mode was used for this study.

Spatial resolution measurements were performed by scanning a thin line source of ^{18}F in air. The data were rebinned using an 8° acceptance window in the NOR mode. Measurement of full width at half maximum (FWHM) was performed on a profile measured transaxially across the reconstructed line source image.

Measurements of volume sensitivity were performed by scanning a 22-cm-diameter cylindrical phantom containing a solution of ^{18}F, as previously described (*17*).

To evaluate the ability of the DHC system to detect lesions with increased uptake, a 22-cm-diameter cylindrical phantom containing six spheres with diameters of 1.3–3.8 cm was used as reported previously (*17*). Both the phantom and the spheres were filled with a solution containing ^{18}F sodium fluoride with the activities adjusted to provide a ratio of sphere activity to background activity of 5:1 and imaged with the DHC system. Spherical lesion-to-background ratios (L/B) were measured from the reconstructed images and plotted along with the data for PET and SPECT that were previously reported (*17*).

FDG PET images were obtained using an eight-ring tomograph with a 12.5-cm axial field of view that produced 15 transaxial images, each 8 mm thick, with a measured reconstructed resolution of 6.5 mm (FWHM) (ECAT 933/08/16; Siemens, Iselin, NJ). The images were reconstructed using photopeak/photopeak counts using an energy window >350 keV. The scanner hardware estimated and corrected for random events by using the standard delayed-window technique. The volume sensitivity was measured with the same technique used for the DHC system.

Patient Population

Twenty-six patients referred for an FDG PET scan between November 1996 and February 1997 (17 men and 9 women; age range 21–71 y, mean ± SD: 53 ± 14 y) were included in the study. Nineteen patients presented with known or suspected malignancies and 7 for cerebral evaluation. All patients fasted for a minimum of 4 h before imaging. None were diabetic.

FDG PET Imaging

The field of view encompassed the chest, abdomen, and pelvis (five-bed sequential positions) for the 19 oncology patients and the brain (two interleaved bed positions) for the 7 neurology patients.

To correct for soft-tissue photon attenuation, transmission scans requiring 10 min per bed position were obtained in 17 of 19 oncology patients using a ring source of ^{68}Ge. After the intravenous administration of approximately 10 mCi (370 MBq) FDG, transaxial emission images were acquired for 15 min per bed position and reconstructed in a 128 × 128 matrix using a Hamming filter with a cutoff frequency of 0.5 cycles per pixel. The uptake period between the injection of FDG and the beginning of emission scanning ranged from 54 to 120 min (mean ± SD: 73 ± 16 min). A stationary laser system was used to ensure accurate positioning between transmission and emission scanning. Body images were corrected for attenuation using the transmission scan and brain images with a calculated geometric attenuation factor using a coefficient of 0.095 cm^{-1}. FDG PET images were available for viewing both with and without attenuation correction.

FDG Imaging Using Positron Coincidence Detection and Dual-Head Gamma Camera

DHC images were acquired for 30 min over the region of interest selected by the findings on CT scan for both body and brain scans. The uptake time between FDG injection and DHC imaging ranged from 27 to 225 min (mean ± SD: 115 ± 68 min).

The images were reconstructed using a Metz filter (power of 3 and FWHM of 10). The body images were not corrected for attenuation, and the brain images were corrected for attenuation with a calculated geometric attenuation using a coefficient of 0.095 cm^{-1}.

This protocol was approved by the institutional review board, and all patients gave their written informed consent.

Image and Data Analysis

FDG PET and DHC images without attenuation correction were viewed on an interactive computer system using both a linear gray scale and a continuous, linear rainbow color scale with varying degrees of background subtraction.

One experienced nuclear medicine physician evaluated the FDG PET images, and two other experienced nuclear medicine physicians interpreted the FDG DHC images individually and separately, without knowledge of the FDG PET results. Clinical data and conventional radiologic images (chest radiographs, CT scans, CT portograms and sonograms) were available when relevant for correlation at the time of interpretation. Regions of focal radiographic abnormality and any region of increased FDG uptake above background that was not located in an area of physiological FDG accumulation were visually scored on a four-point grading

system, as in a previous study performed in our laboratory (*17*): no uptake (grade 0), equivocal uptake (grade 1), mild uptake (grade 2) or definitely increased uptake (grade 3).

Large clusters of lesions have been counted as one lesion, because when many lesions are close together they are impossible to resolve and count individually. In such instances, it is common practice to refer to them as lymph node regions or anatomic sites that make a difference in staging or management (*20–22*). As shown in Table 1, involvement of all anatomic sites has been detected by both DHC and PET when the size of the lesion was referred to as a "cluster."

Semiquantitative evaluation was performed on the attenuation-corrected FDG PET images. Using the average activity per pixel in the region of maximal FDG, uptake in a lesion (approximate size of region of interest, 1 cm^2), the standardized uptake value (SUV = tumor activity concentration [μCi/mL]/dose injected [mCi]/body weight [kg]) was calculated for lesions in the oncology patients. L/Bs were calculated for liver and lung lesions. Regional background activities were determined by calculating the average activity per pixel in a region of surrounding normal tissue. Because of the inaccuracies of volume averaging in lesions less the 1.0 cm in diameter, SUV and L/B were not calculated for these small lesions. Image findings were also correlated with histological and/or clinical follow-up (8–12 mo) in all patients. As in our previous study, activity rated as grade 2 or 3 was considered positive for pathological uptake (*17*). For the patients with brain

TABLE 1
Oncology Patients

Patient	Lesion	Site on CT	Size on CT (cm)	SUV	L/B	Grade on FDG PET	Grade on FDG DHC	History
A	1	Mediastinum	Large cluster	NA	NA	3	3	Hodgkin's lymphoma
	2	Abdominal nodes	Large cluster	NA	NA	3	3	
	3	Retroperitoneal nodes	Large cluster	NA	NA	3	3	
	4	Spleen	Large cluster	NA	NA	3	3	
B*	5	Pancreas*	3.0	4.3	NA	3	3	Pancreatic carcinoma
	6	Liver*	1.0	3.0	2.2	3	1	
C	7	Lung	2.0	6.3	9.4	3	3	Lung carcinoma
D*	8	Liver (hilum)*	1.8	5.5	2.6	3	1	Colon carcinoma
	9	Liver*	3.0	4.5	2.2	3	3	
	10	Liver*	2.2	6.4	3.1	3	3	
E*	11	Liver*	Cluster	5.9	2.7	3	3	Cholangiocarcinoma
	12	Mediastinum	3.0	4.7	2.8	3	3	
F	13	Rectum	7.0	8.2	NA	3	3	Colon carcinoma
	14	Liver	3.0	5.8	4.2	3	3	
	15	Liver (central)	3.0	3.9	2.8	3	1	
	16	Liver (central)	2.5	3.5	2.5	3	1	
G	17	Liver	4.0	7.0	3.1	3	3	Colon carcinoma
	18	Liver	2.5	7.4	3.3	3	3	
	19	Liver	2.5	7.4	3.3	3	3	
H*	20	Neck node*	0.7	NA	NA	3	0	Thyroid carcinoma
I*	21	Liver*	2.0	7.6	2.6	3	3	Colon carcinoma
	22	Liver*	1.2	4.5	1.6	3	1	
J	23	Liver	4.0	9.4	2.2	3	3	Colon carcinoma
K*	24	Lung*	2.5	5.8	15.0	3	3	Colon carcinoma
	25	Retroperitoneal* nodes	2.0	8.3	NA	3	3	
L*	26	Liver*	5.0	9.9	2.8	3	3	Colon carcinoma
M	27	Liver	2.0	6.4	2.7	3	3	Esophageal carcinoma
	28	Liver	1.5	7.1	3.0	3	3	
	29	Liver	1.0	6.7	2.8	3	2	
	30	Liver	1.0	5.2	2.2	3	1	
N		No lesion						Hodgkin's lymphoma, post therapy
O	31	Liver	5.0	6.3	5.3	3	3	Colon carcinoma
	32	Liver	2.0	2.9	2.4	2	0	
	33	Liver	3.0	3.8	3.2	3	3	
P*	34	Liver*	2.5	7.3	3.6	3	1	Colon carcinoma
Q		No lesion						Melanoma, post therapy
R	35	Lung	5.0	3.3	7.3	3	3	Lung carcinoma
	36	Lung	0.7	1.3	2.9	2	0	
	37	Lung	1.6	3.3	7.4	3	3	
S	38	Lung	6.0	19.6	25.0	3	3	Lung carcinoma

*Metastasis (n = 13) in 8 patients confirmed by pathology.

SUV = standardized uptake value; L/B = lesion-to-background ratio; FDG = fluorodeoxyglucose; DHC = dual-head gamma camera; NA = not available.

disorders, a ratio of activity from abnormal-to-normal region was calculated. These regions were chosen according to the patient's disorder. These ratios obtained on the PET and DHC images were compared by linear regression analysis.

RESULTS

Physical Measurements

A spatial resolution value of 4.5 mm FWHM was measured in air for the DHC system and 6.5 mm for the PET system. Sensitivity measurements for the camera system in the NOR mode were determined to be 89 coincidences/min/μCi. For the PET system, the measured sensitivity was 2238 coincidences/min/μCi.

Plots of L/Bs versus simulated lesion diameters obtained from phantom measurements are shown in Figure 1. These data show that lesion detectability with DHC is very close to that of high-energy SPECT for L/B activity ratios of 5:1. Both are inferior to that of PET. Using a contrast ratio of 1.3 as the minimum detectable lesion contrast as previously defined (*17*) and extrapolating the data to a lesion diameter of 0 (contrast ratio, 1.0) these data predict limits of detectability of 0.4, 1.35 and 1.5 cm for PET, DHC and high-energy collimated SPECT, respectively.

Imaging variables in patient examinations—such as increased information density, decreased organ uptake or increased lesion uptake—may decrease the minimum detectable lesion size predicted with these phantom measurements.

Clinical Results

In the patient imaging protocol, a 30-min acquisition was used with the scintillation camera. Because this imaging procedure typically followed the PET scan, this was the maximum imaging time that the patient could tolerate before movement would potentially compromise the image quality. This resulted in marginal counting statistics in some of the images. The total coincidence in the patient's datasets ranged from 583,915 to 2,320,009, with an average of 1,183,998. Random coincidence ranged from 4% to 29% of the total, with an average of 14%.

For oncology patients (n = 19), the clinical results are shown in Table 1. Thirty-eight lesions were detected on PET images (grades 2 or 3). On CT, these lesions ranged from 0.7 to 5.0 cm. Of these 38 lesions, 28 (73%) were identified on DHC images. Among the 10 lesions that were not seen on the DHC images, 5 were small (<1.2 cm), 2 were located centrally and suffered from increased soft-tissue attenuation and 3 were located in close proximity to physiological activity in the gastrointestinal tract. Seven of these 10 undetected lesions were graded as equivocal, because they could be retrospectively identified after correlation with PET images. If only lesions greater than 1.2 cm are considered, DHC imaging detected 28 of 33 (85%) of the lesions. If more lesions were counted in the 2 patients with clusters of lesions, both PET and DHC would have a higher detection rate. If the 2 patients with clusters of lesions are not taken into consideration, 33 lesions would be detected by PET and 23 of 33 (70%) by DHC imaging. Figure 2 shows a typical example of a patient with Hodgkin's lymphoma with multiple lesions detected by both techniques (patient A). Figure 3 shows images of a patient with pancreatic carcinoma seen by both techniques; however, PET images also showed a small lesion in the left lobe of the liver, but the DHC images were equivocal in showing that small metastasis (patient B). Eight of the 19 patients had biopsies or surgery, and their 13 lesions identified by PET were confirmed as malignant. Five of them were not identified on DHC images.

The study was not designed to perform a comparison between CT and PET or CT and DHC. In many institutions, as well as in this study, PET images are routinely obtained over the chest, abdomen and pelvis in patients with body tumors, leading to detection of unsuspected metastases in anatomic regions outside the field of view of the routine imaging studies obtained as part of the standard of care. In this study, because of the length of total imaging time (PET plus DHC) for the patient, DHC was not performed over the entire body but over a region of interest selected according to the findings on CT scan. Therefore, the comparison with

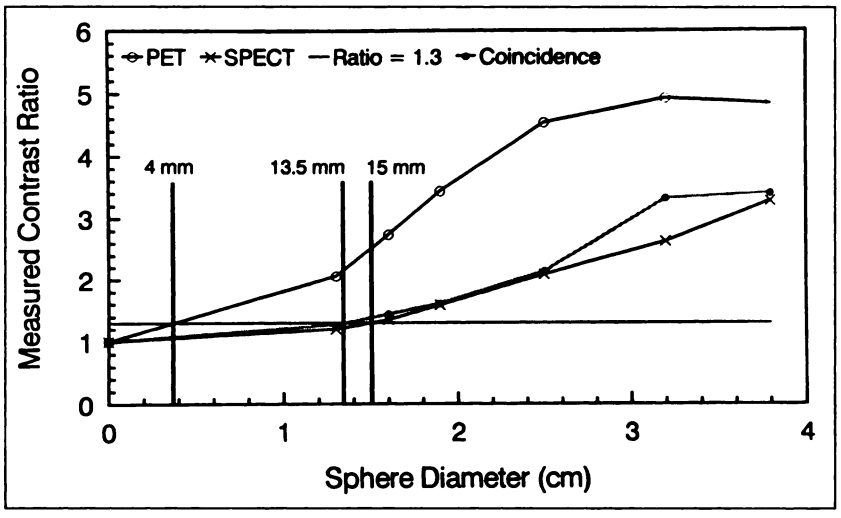

FIGURE 1. Plot of L/Bs with dual-head scintillation camera using DHC with 3/8-in-thick NaI(Tl) crystal, with region-of-interest calculations for spherical lesions, 1.3–3.8 cm in diameter, in activity-filled background contained in 22-cm-diameter cylindrical phantom. Activity of ^{18}F sodium fluoride in lesions and background was adjusted to provide ratio of 5:1. Data obtained using FDG PET with 5:1 ratio are provided for comparison. Horizontal line represents L/B of 1.3:1.0 to define minimum ratio that can be visualized.

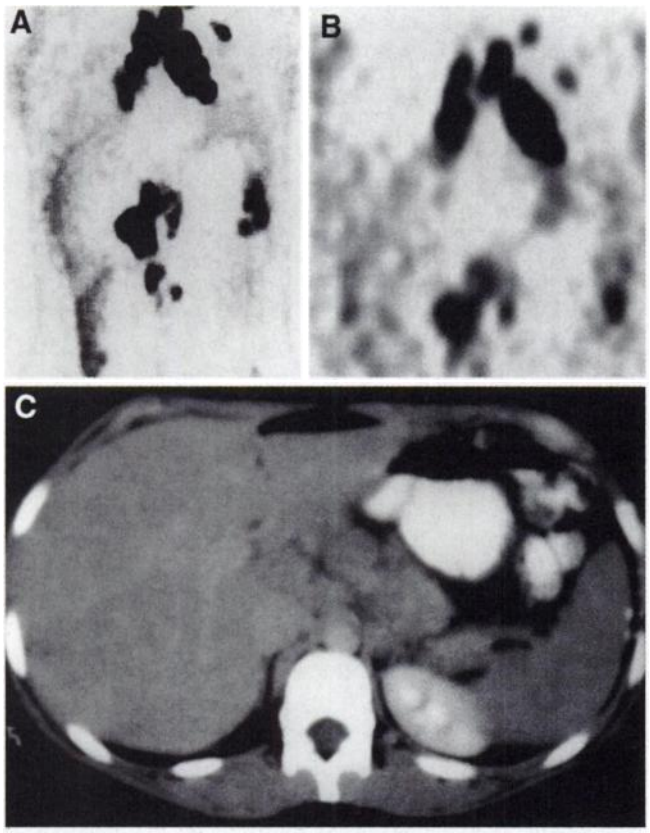

FIGURE 2. A 21-y-old woman with Hodgkin's lymphoma. Coronal PET (A) and DHC (B) images show similar foci of increased uptake indicating lymph nodes involved by lymphoma (patient A). (C) CT shows retroperitoneal lymph nodes.

CT can be done only within the field of view of the DHC images. Among the 38 lesions with FDG uptake on PET images, 33 were interpreted as malignant on CT, 3 were indeterminate pulmonary nodules (lesions 24, 36, and 37 in Table 1), and 2 were unsuspected metastases detected by PET, which guided the performance of a thin-slice CT scan showing corresponding small lesions (lesions 6 and 20 in Table 1). Both were confirmed pathologically as metastases. Surgery was canceled for the patient with pancreatic carcinoma with the small liver metastasis, and the patient with papillary carcinoma of the thyroid underwent left neck dissection, which showed one lymph node involved by tumor. Of the 5 indeterminate lesions on CT, DHC identified 2 pulmonary metastases.

The clinical results of the neurology patients (n = 7) are shown in Table 2. Four patients were evaluated for dementia, 1 for epilepsy and 2 for mass lesions. The region of interest was chosen for semiquantitative evaluation according to the findings. The correlation coefficient between semiquantitative indices measured on PET and DHC images is 0.93, and the final interpretation was similar for both techniques. Figure 4 (patient Y) shows decreased uptake in the head of the right caudate, corresponding to the gadolinium-enhancing lesion on MRI and leading to the diagnosis of toxoplasmosis rather than lymphoma in a human immunodeficiency virus–positive patient.

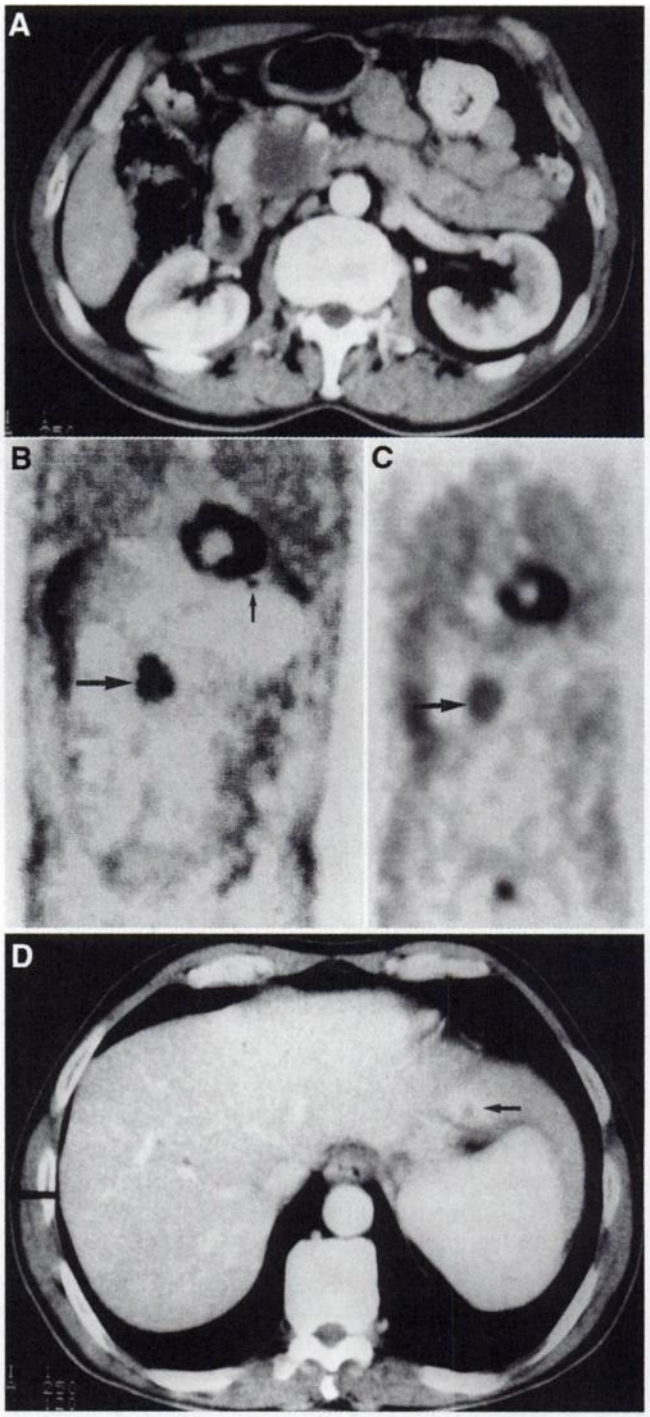

FIGURE 3. A 45-y-old man with history of biliary obstruction. (A) CT shows 3-cm lesion in head of pancreas (large arrow). (B) Coronal PET images clearly show increased uptake in pancreatic lesion and additional focus in left lobe of liver (small arrow). (C) Coronal DHC images show definite uptake only in pancreatic lesion (large arrow). (D) Repeat CT confirmed small lesion in left lobe of liver (patient B, small arrow).

DISCUSSION

A variety of malignant tumors avidly accumulate FDG, due, in part, to increased numbers of glucose transporter proteins and enzyme levels that promote glycolysis (*23,24*).

TABLE 2
Patients with Brain Disorders

Patients	History	MRI	Ratio	Ratio PET	Ratio DHC	Interpretation
T	Dementia	NA				Normal
U	Dementia	Normal	BG/TH	0.80	0.93	Equivocal
V	Dementia	Cerebellar atrophy	Cerebellum/BG	0.42	0.33	Cerebellar dysfunction
W	Dementia	Normal	Posterior cortex/BG	0.51	0.67	Alzheimer's disease
X	Epilepsy	NA	Temporal cortex-to-asymmetry index	0.09	0.22	Right temporal focus
Y	HIV+/lesion	Right BG (2 cm)	BG-to-asymmetry index	0.30	0.33	Right BG abscess
Z	Lesions	Multiple (1–2 cm)		Equivocal	Artifact	Equivocal

DHC = dual-head coincidence gamma camera; NA = not available; BG = basal ganglia; TH = thalamus; HIV = human immunodeficiency virus.

We have previously shown that, despite the limited spatial resolution of 511-keV collimated SPECT (17 mm), FDG SPECT imaging is adequate to detect primary and metastatic lesions larger than 1.8 cm in diameter and to differentiate benign from malignant lesions (*17*). Using this technique, post-therapy changes also can be differentiated from tumor recurrence by the lower uptake of FDG seen. Another group of investigators evaluated 26 patients with indeterminate lung nodules using a dual-head SPECT gamma camera equipped with 511-keV collimators. They reported a sensitivity of 81% to detect malignant nodules, with no false-negatives in lesions greater than 2 cm, but four false-negatives in five lesions smaller than 2 cm (*19*). The inability to accurately detect lesions of less than 1.8 cm stimulated the development of DHC imaging, which offers enhanced resolution. Because DHC imaging is a collimator-less three-dimensional volumetric procedure, it is a technique that potentially enables the detection of lesions of only a few millimeters. The spatial resolution is limited only by the intrinsic resolution of the camera. However, in spite of the improved resolution of DHC, the data presented in this study comparing FDG DHC imaging with a ⅜-in.-thick NaI(Tl) crystal and PET show that DHC imaging was not superior to FDG SPECT with ultrahigh-energy collimators for the detection of small lesions. DHC is, however, quite accurate in the detection of malignant lesions larger than 1.8 cm.

In brain imaging applications, it was apparent that the ultrahigh-energy parallel-hole collimators used for SPECT acquisition did not have adequate spatial resolution to provide diagnostically acceptable images. A set of ultrahigh-energy fanbeam collimators was designed and fabricated incorporating smaller diameter, longer holes and thinner septa to provide improved spatial resolution without degrading sensitivity (*25*). In spite of the improvement in both spatial resolution and sensitivity with the ultrahigh-energy fanbeam collimators, diagnostic quality brain images could

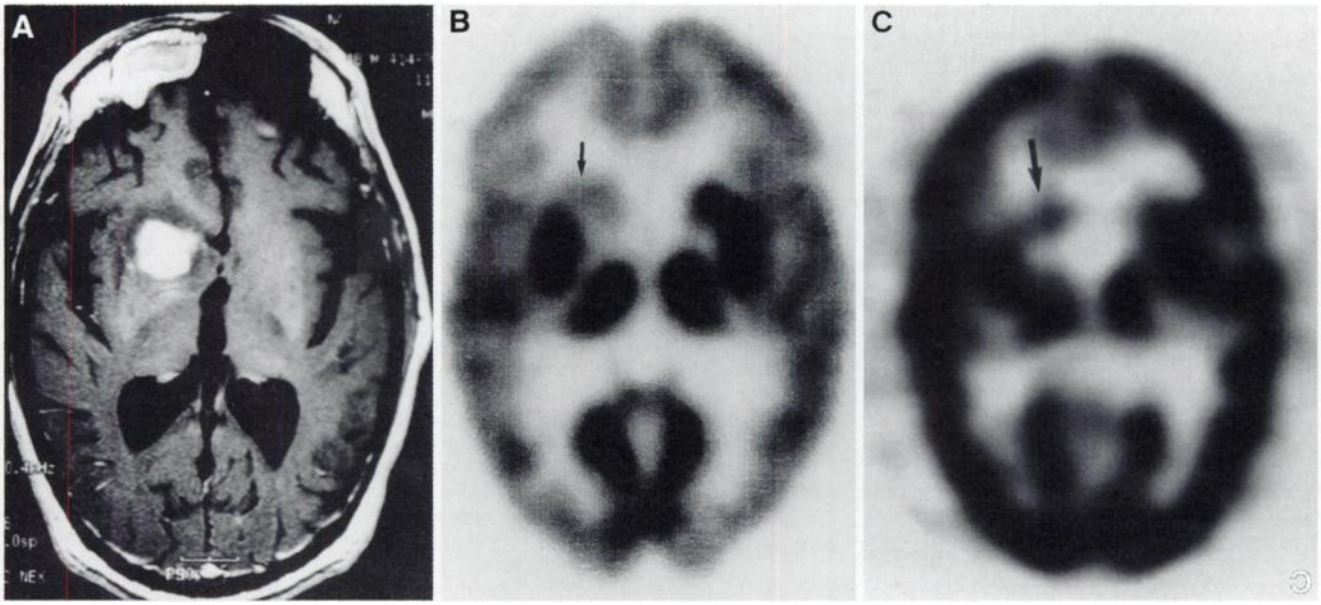

FIGURE 4. 49-y-old HIV-positive man presented with change in mental status accompanied by sinusitis. Gadolinium-enhanced T_1-weighted MR image (A) shows enhancing lesion in head of right caudate nucleus. Both PET (B) and DHC (C) images show decreased uptake in same location, indicating toxoplasmosis rather than lymphoma (patient Y, arrows).

not be consistently obtained, because of the length of the acquisition protocol (40–60 min). A significant improvement in brain image quality has been achieved by the introduction of DHC imaging, as shown in this study.

In this study, we have shown that FDG imaging using DHC with a conventional gamma camera greatly improves the resolution of the system compared with FDG SPECT imaging with ultrahigh-energy collimators. The detection rate for malignant lesions, however, appears to be similar with both techniques. This is most probably related to the limited sensitivity of the DHC system. The limited detection rate using DHC in patients with oncological disease has also been reported by other investigators with a system developed by a different manufacturer using a ⅝-in.-thick crystal and dynamic segmentation (*26*). These investigators reported difficulty in detecting lesions smaller than 1.5 cm, both in the abdomen and pelvis, compared with PET (*26*).

Limitations of the Study

FDG DHC imaging was performed an average of 115 min after FDG administration. Because of the short half-life of ^{18}F, this delay resulted in a noticeable decrease in the information density available for the FDG DHC acquisition compared with the FDG PET acquisition. The average FDG dose present in the patient at the start of imaging, not taking into account the biological excretion, was 6.75 mCi at the start of PET imaging and 5.2 mCi at the start of DHC imaging. The combination of the limited counting rate and reduced sensitivity of the FDG DHC system compared with the PET system may have compromised the visualization of some of the smaller and deeper lesions. This may be more relevant when using slit collimators compared with cameras with no collimators using three-dimensional data acquisition techniques.

The thickness of the crystal of the DHC used in this study (⅜ versus ½ or ⅝ in.) is another limitation, because of its poor sensitivity to detect 511-keV photons. Clinical trials are currently ongoing at Vanderbilt and Duke Universities to assess the difference in lesion detectability and improvement in image quality using thicker NaI(Tl) crystals.

The third limitation is the reconstruction algorithm used in this study; filtered backprojection amplifies the statistical noise that adversely affects image quality. New algorithms using iterative reconstruction have been developed for coincidence imaging that provides good signal-to-noise ratio in a timely fashion (*27*). Iterative reconstruction was not available at the time of this study. It is currently being evaluated on newly acquired sets of images in another series of patients.

The fourth limitation is the lack of attenuation correction for the body DHC images, making detection of centrally located lesions difficult.

A fifth limitation of the study is the model of PET scanner used, ECAT 933/08/16, which was developed in the late 1980s. The spatial resolution, axial field of view and other specifications of positron scanners have improved considerably over the past decade.

CONCLUSION

Preliminary results comparing FDG DHC imaging using a prototype DHC with PET in a series of patients have shown this to be a promising technique for assessing patients with a variety of brain and oncological diseases. Although the spatial resolutions of PET with a dedicated PET scanner and of DHC are in the same range, the lesion detectability remains superior with PET (4 mm for PET versus 13.5 mm for DHC in phantom experiments), with contrast ratios of 5:1. This is most probably attributable to the higher sensitivity of PET (2238 coincidences/min/μCi for PET versus 89 coincidences/min/μCi for DHC). In patients, DHC detected 73% of the lesions identified by PET. This can be explained by the limited sensitivity of ⅜-in.-thick NaI(Tl) crystals to detect 511 keV, the suboptimal reconstruction algorithm (filtered backprojection), the lack of attenuation correction and the suboptimal start of imaging time for DHC images. Further developments in gamma camera front end technology, thicker NaI(Tl) crystals, new crystal compounds, iterative reconstruction and attenuation correction are under investigation and offer exciting possibilities for the future.

With decreasing cost and enhanced distribution of FDG, the availability of gamma cameras to provide collimated high-energy and DHC imaging, as well as maintaining their ability to perform routine scintigraphic studies, should increase in the future and make FDG imaging more cost effective.

ACKNOWLEDGMENTS

We want to thank Dawn Shone and Mary Stoner for their technical support, Adi Balan and Naor Weiner for their help with the physical measurements, John Bobbit for preparation of the illustrations and Donna Wagner and Tom Ebers for preparation of the article.

REFERENCES

1. DeChiro G. Positron emission tomography using ^{18}F-fluorodeoxyglucose in brain tumors. *Invest Radiol.* 1987;22:360–371.
2. Coubes P, Awad IA, Antar M, Magdinec M, Sufka B. Comparison and spatial correlation of interictal HMPAO-SPECT and FDG-PET in intractable temporal lobe epilepsy. *Neurol Res.* 1993;15:160–168.
3. Weinstein HC, Scheltens P, Hijdra W, van Royen EA. Neuro-imaging in the diagnosis of Alzheimer's disease, II. Positron and single photon emission tomography. *Clin Neurol Neurosurg.* 1993;95:81–91.
4. Tillisch J, Brunken R, Marshall R, et al. Reversibility of cardiac wall-motion abnormalities predicted by positron tomography. *N Engl J Med.* 1986;314:884–888.
5. Bonow RO, Dilsizian V, Cuocolo A, Bacharach SL. Identification of viable myocardium in patients with chronic coronary artery disease and left ventricular dysfunction: comparison of thallium scintigraphy with reinjection and PET imaging with ^{18}F-fluorodeoxyglucose. *Circulation.* 1991;83:23–67.
6. Altehoefer C, Kaiser HJ, Dorr R, et al. Fluorine-18-deoxyglucose PET for assessment of viable myocardium in perfusion detects in ^{99m}Tc-MIBI SPECT: a comparative study in patients with coronary artery disease. *Eur J Nucl Med.* 1992;19:334–342.
7. Wahl RL. Positron emission tomography: applications in oncology. In: Murray IPC, Ell PJ, eds. *Nuclear Medicine in Clinical Diagnosis and Treatment.* Edinburgh, Scotland: Churchill Livingstone, 1994:801–820.
8. Conti PS, Keppler JS, Halls JM. Positron emission tomography: a financial and operational analysis. *AJR.* 1994;162:1279–1286.

9. Gambhir SS, Hoh CK, Phelps ME, Madar I, Maddahi J. Decision tree sensitivity analysis for cost-effectiveness of FDG PET in the staging of non-small-cell lung carcinoma. *J Nucl Med.* 1996;37:1428–1436.
10. Valk PE, Pounds TR,Tesar RD, Hopkins DM, Haseman MK. Cost-effectiveness of PET imaging in clinical oncology. *Nucl Med Biol.* 1996;23:737–743.
11. Drane WE, Abbott FD, Nicole MW, Mastin ST, Kuperus JH. Technology for FDG SPECT with a relatively inexpensive gamma camera. *Radiology.* 1994;191:461–465.
12. Van Lingen A, Huijgens PC, Visser FC, et al. Performance characteristics of a 511-keV collimator for imaging positron emitters with a standard gamma camera. *Eur J Nucl Med.* 1992;19:315–321.
13. Burt RA, Perkins OW, Oppenheim BE, et al. Direct comparison of fluorine-18-FDG SPECT, fluorine-18-FDG PET and rest thallium-201 SPECT for detection of myocardial viability. *J Nucl Med.* 1995;36:176–179.
14. Macfarlane DJ, Cotton L, Ackermann RJ, et al. Triple-head SPECT with 2-[fluorine-18]fluoro-2-deoxy-D-glucose (FDG): initial evaluation in oncology and comparison with FDG PET. *Radiology.* 1995;194;425–429.
15. Martin WH, Delbeke D, Patton JA, et al. FDG SPECT: correlation with FDG PET. *J Nucl Med.* 1995;36:988–995.
16. Delbeke D, Videlefsky S, Patton JA, et al. Rest myocardial perfusion/metabolism imaging using simultaneous dual-isotope acquisition SPECT wth technetium-99m-MIBI/fluorine-18-FDG. *J Nucl Med.* 1995;36:2110–2119.
17. Martin WH, Delbeke D, Patton JA, Sandler MP. Detection of malignancies with SPECT versus PET, with 2-[fluorine-18]fluoro-2-deoxy-D-glucose. *Radiology.* 1996;198:225–231.
18. Sandler MP, Videlefsky S, Delbeke D, et al. Evaluation of myocardial ischemia using a rest metabolism/stress perfusion protocol with fluorine-18-deoxyglucose/technetium-99m-MIBI and dual-isotope simultaneous-acquisition single-photon emission computed tomography. *J Am Coll Cardiol.* 1995;26:870–878.
19. Worsley DF, Celler A, Adam MG, et al. Pulmonary nodules: differential diagnosis using ^{18}F-fluorodeoxyglucose single-photon emission computed tomography. *AJR.* 1997;168:771–774.
20. Moog F, Bangerter M, Diederichs CG, et al. Lymphoma: role of whole-body 2-deoxy-2-[F-18]fluoro-D-glucose (FDG) PET in nodal staging. *Radiology.* 1997; 203:795–800.
21. Hoh CK, Glaspy J, Rosen P, et al. Whole-body FDG PET imaging for staging of Hodgkin's disease and lymphoma. *J Nucl Med.* 1997;38:343–348.
22. Newman JS, Francis IR, Kaminski MS, Wahl RL. Imaging of lymphoma with PET with 2-[F-18]-fluoro-2-deoxy-D-glucose: correlation with CT. *Radiology.* 1994;190:111–116.
23. Flier JS, Mueckler MM, Usher P, Lodish HF. Elevated levels of glucose transport and transporter messenger RNA are induced by rats or src oncogenes. *Science.* 1987;235:1492–1495.
24. Monakhov NK, Neistadt EL, Shavolvskil MM, et al. Physiochemical properties and isoenzyme composition of hexokinase from normal and malignant human tissues. *J Natl Cancer Inst.* 1978:61:27–34.
25. Patton JA, Sandler MP, Ohana I, Weinfeld Z. High-energy (511-keV) imaging with the scintillation camera. *RadioGraphics.* 1996;16:1183–1194.
26. Shreve P, Steventon RS, Deters E, Gross MD, Wahl RL. FDG imaging of neoplasms using a dual-head SPECT camera operated in coincidence mode. *Eur J Nucl Med.* 1997;24:860.
27. Shepp LA, Vardi Y. Maximum likelihood reconstruction for emission tomography. *Trans Med Imaging.* 1982;M-13:100–108.